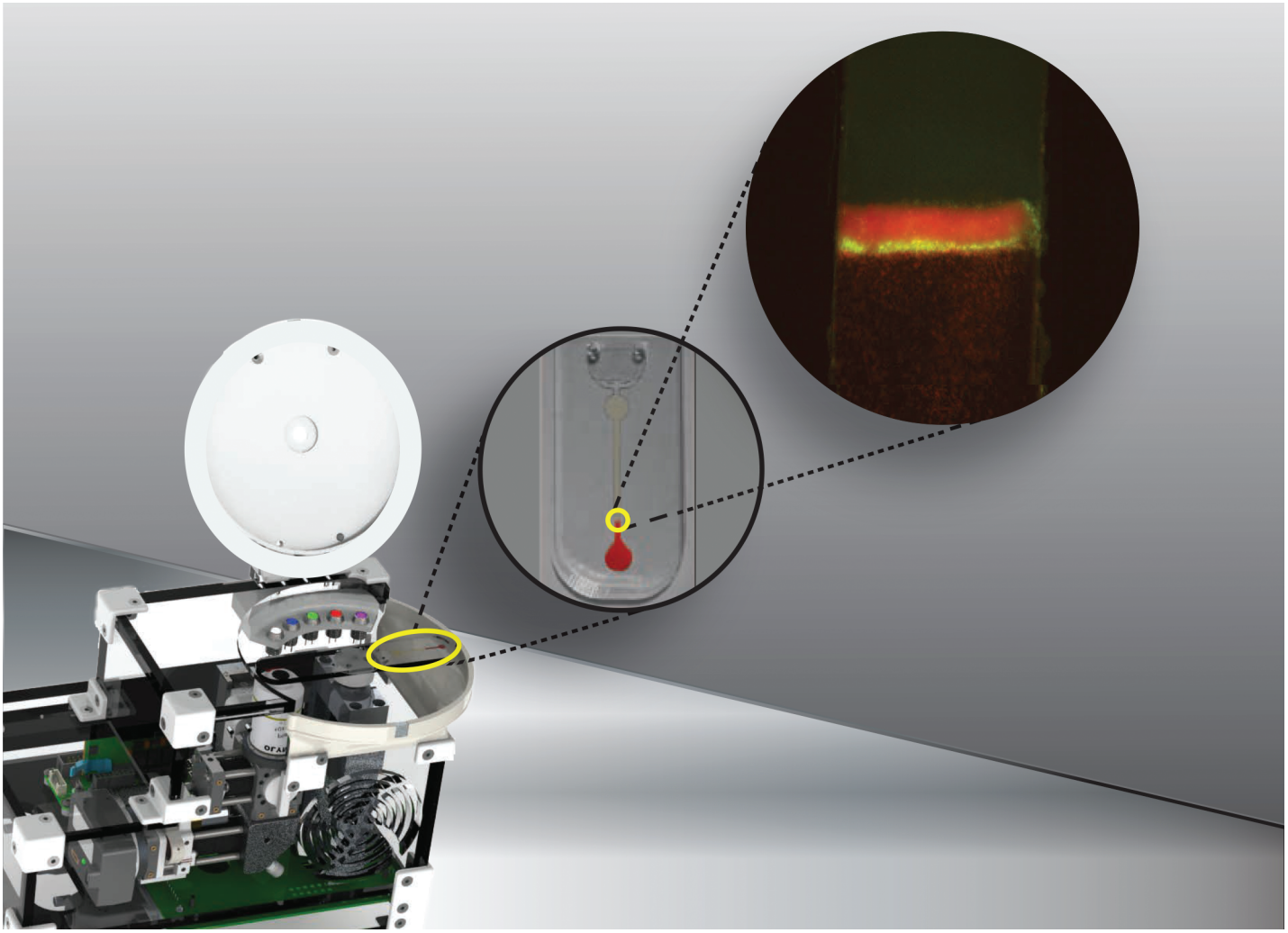

Showcasing research from Max L. Balter and colleagues from Rutgers University, VascuLogic LLC, and Massachusetts General Hospital, USA.

Differential leukocyte counting via fluorescent detection and image processing on a centrifugal microfluidic platform

We present two methods for enumerating leukocytes on a centrifugal platform using a custom-built fluorescent microscope, nuclear staining, and image processing. A bulk-cell analysis approach correlates the pixel areas of fractionated lymphocyte/monocyte and granulocyte layers with cell counts. Analyzing the pixel intensities of the fluorescing white cell region, we can differentiate lymphocytes from monocytes via pixel clustering, demonstrating a 3-part differential. This is a simple, reliable method with minimal sample preparation in a portable unit.

As featured in:

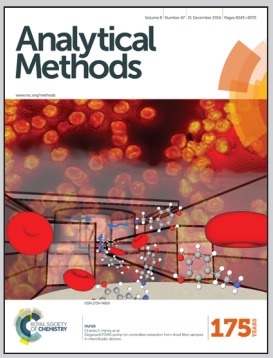

See Max L. Balter *et al.*, *Anal. Methods*, 2016, **8**, 8272.

ROYAL SOCIETY OF CHEMISTRY

www.rsc.org/methods

Registered charity number: 207890

Analytical Methods

PAPER

Cite this: *Anal. Methods*, 2016, **8**, 8272

Differential leukocyte counting *via* fluorescent detection and image processing on a centrifugal microfluidic platform†

Max L. Balter,*[a] Alvin I. Chen,[a] C. Amara Colinco,[a] Alexander Gorshkov,[a] Brian Bixon,[a] Vincent Martin,[a] Alexander Fromholtz,[a] Timothy J. Maguire[b] and Martin L. Yarmush[ac]

Received 19th September 2016
Accepted 24th October 2016

DOI: 10.1039/c6ay02614a

www.rsc.org/methods

Centrifugal microfluidics has received much attention in the last decade for the automation of blood testing at the point-of-care, specifically for the detection of chemistries, proteins, and nucleic acids. However, the detection of common blood cells on-disc, particularly leukocytes, remains a challenge. In this paper, we present two methods for enumerating leukocytes on a centrifugal platform using a custom-built fluorescent microscope, nuclear staining, and image processing. In the first method, cell analysis is performed in glass capillary tubes; in the second, acrylic chips are used. A bulk-cell analysis approach is implemented in both cases where the pixel areas of fractionated lymphocyte/monocyte and granulocyte layers are correlated with cell counts. Generating standard curves using porcine blood sample controls, we observed strong linear fits to measured cell counts using both methods. Analyzing the pixel intensities of the fluorescing white cell region, we are able to differentiate lymphocytes from monocytes *via* pixel clustering, demonstrating the capacity to perform a 3-part differential. Finally, a discussion of pros and cons of the bulk-cell analysis approach concludes the paper.

1 Introduction

Diagnostic blood testing is the most common medical routine performed in the world and in many ways, forms the cornerstone of modern medicine.[1] In the U.S., blood tests are performed 2 billion times each year and influence 80% of medical decisions made in hospital and primary care settings.[2] However, diagnostic results are generated almost exclusively in centralized labs from large-volume blood samples. This approach requires the transport of samples to a centralized facility and highly trained personnel to run the analyses on bench-top instruments, resulting in long turnaround times on the order of hours to days.[3] Unexpected delays can also arise, further prolonging the time from sample-to-answer.

Point-of-care testing has shown the potential to reduce turnaround times and expedite the clinical decision making process.[4] Yet despite the commercialization of a wide range of analyzers, these devices are used for less than 10% of all blood tests.[5] One limitation with these devices is that they only perform a narrow set of assays. However, a study of the testing patterns in the emergency department at Massachusetts General Hospital in the U.S. showed that diagnostic tests are not ordered individually, but nearly always in combination with other panels.[6,7] For example, patients that showed symptoms for chest pain, seizure, or abdominal pain had blood tests for cell counts, chemistries, and proteins. In order to perform these tests, multiple instruments and blood samples would be required. This lack of integration with different assays is a major drawback for current systems.

Over the last decade, centrifugal microfluidics has emerged as a niche platform, providing key features that make it ideally suited for integrating a range of blood tests on one self-contained chip. Here, all steps from sample preparation to analysis can be automated by controlling the speed of the centrifuge motor:[8–10] reagent storage and release,[11] sedimentation and plasma extraction,[12,13] liquid transport and pumping,[14,15] metering and valving,[16,17] mixing and washing,[18] and analyte detection.[19] Also, centrifugal microfluidics obviates the need for external pumps or robotic pipettes to manipulate samples and reagents—resulting in a compact device that can be used in decentralized settings.

The majority of research in centrifugal microfluidics has focused on the detection of chemistries,[20,21] proteins,[22,23] nucleic acids,[24,25] and rare cells,[26,27] with several analyzers entering the market. For example, the Abaxis Piccolo Xpress device

[a]*Rutgers University, Department of Biomedical Engineering, Piscataway, NJ, 08854, USA. E-mail: balterm53@gmail.com; Fax: +1-732-445-3753; Tel: +1-617-721-2064*

[b]*VascuLogic LLC, Piscataway, NJ, 08854, USA*

[c]*Massachusetts General Hospital, Boston, MA, 02108, USA*

† Electronic supplementary information (ESI) available: Detailed descriptions of the image processing algorithms and corresponding Matlab code. See DOI: 10.1039/c6ay02614a

automates the detection of chemistries,[28] and the Samsung LabGEO IB10 performs automated immunoassays.[29] However, the enumeration of common cells on-disc, particularly leukocytes, remains a challenge.[30] The diagnostic value of leukocyte counts cannot be overstated as they provide clinicians with key information regarding patient health, especially when diagnosing the common flu (high lymphocyte count) or bacterial infection (high granulocyte count).

1.1 Previous work on leukocyte counting

Several groups have described centrifugal microfluidic systems for leukocyte isolation and detection. Shiono *et al.* presented a device for continuous white blood cell (WBC) separation by density gradient centrifugation.[31] Here, a series of Percoll dilutions were continuously introduced to the spinning disc to fractionate the buffy coat into three sub-types (*i.e.*, lymphocytes (lym), monocytes (mon), and granulocytes (gran)). Despite promising separation efficiency, the system was reported to take up to two hours to process blood samples, and detection was performed off-disc. Schaff *et al.* provided proof-of-concept for differential leukocyte counting *via* centrifugal microfluidics using two cell lines with different densities (K562 and Jurkat cells).[32] However, no cell quantification data was presented to evaluate the accuracy of this method. More recently, Kinahan *et al.* demonstrated the use of pneumatic siphon valving and density-gradient medium to extract leukocytes from whole blood.[33] Nevertheless, the device only exhibited a leukocyte extraction efficiency of 34% compared to hospital laboratory data. Furthermore, detection was performed off-chip and no differential data was reported.

Apart from disc-based devices, there are several commercial point-of-care analyzers that perform leukocyte counting, such as the HemoCue WBC and QBC Star Analyzer. The HemoCue device uses a static cell counting approach based on imaging and enumerating leukocytes stained with methylene blue.[34] Recently, HemoCue has extended this approach to extract a 5-part differential *via* image processing techniques.[35] However, this device is still awaiting FDA approval, and the accuracy of this method remains unclear. Conversely, the QBC Star Analyzer uses a bulk-cell analysis approach in glass capillary tubes, where the thickness of the buffy layers is correlated with a 2-part leukocyte differential.[36,37] The system is also capable of performing hemoglobin, hematocrit, and platelet measurements.

Nevertheless, the device is rather bulky (*i.e.*, 41 × 41 × 41 cm), a number of manual steps are required to process the sample, and the reliability of the system is unclear under varying conditions (*e.g.*, different tube orientations).

In this paper, we present two different methods for differential leukocyte counting using a bulk-cell analysis approach (Fig. 1). In the first method, we use glass capillary tubes to house the blood sample as a control group, similar to the QBC Star Analyzer. We then fractionate the sample using a benchtop centrifuge and analyze the leukocytes on a custom-built fluorescence microscopy station. In the second method, layered acrylic chips are used, but in this case, samples are spun on a miniaturized centrifuge which is further integrated with the microscope. The capillary tube control group allows the acrylic chip results to be compared against an established method.

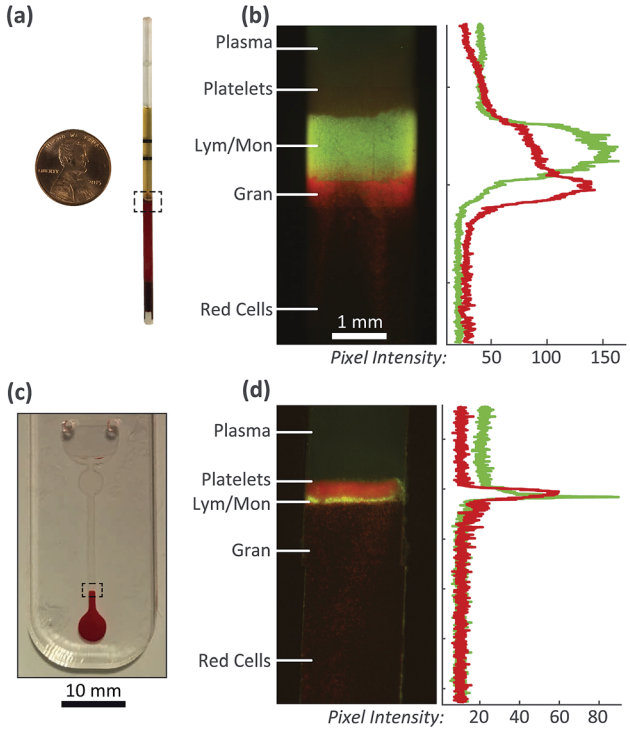

Fig. 1 Differential leukocyte counting using bulk-cell analysis. (a) Capillary tube after centrifugation with the buffy coat outlined. (b) Microscopic image of the buffy coat, highlighting the separated blood layers, and corresponding fluorescent profiles on the right. (c) Acrylic chip after centrifugation, and (d) microscopic image of the buffy coat with corresponding fluorescent profiles on the right.

The paper is outlined as follows. First, Section 2 introduces the leukocyte staining methodology, designs for the fluorescent microscope, and image processing steps implemented to extract and measure the leukocyte region (*i.e.*, the buffy coat). Section 3 presents the results, comparing the buffy coat areas with measured cell counts to generate a set of standard curves for absolute leukocytes and a 2-part differential (*i.e.*, lym/mon and gran) using capillary tubes and acrylic chips. We also demonstrate the use of pixel clustering to separate lymphocytes from monocytes, extending the bulk-cell analysis approach to a 3-part differential. Finally, Section 4 discusses various ways to enhance the accuracy and repeatability of this approach.

2 Experimental materials & methods

Our approach for cell counting utilizes density centrifugation to isolate and enumerate leukocyte sub-types. After centrifugation, distinct bands are formed where cells are layered from most to least dense. Since leukocytes contain nuclei, it is possible to differentially stain them and analyze the distinct layers using fluorescence imaging. The imaged layers can then

be correlated to cell counts with the capacity to perform a 2-part differential, and potentially a 3-part differential, by separating monocytes from lymphocytes based on their fluorescence intensity profiles.

Some advantages of the bulk-cell analysis approach include the following. First no dilution step is required; therefore, it is possible to use whole blood. Second, minimal sample processing is needed with the use of a single nuclear stain—acridine orange (AO). Third, results can be obtained in under 5 min (*i.e.*, the time needed to fractionate the blood sample).

2.1 Leukocyte staining methodology

AO has several unique biochemical characteristics that enable the differentiation of leukocytes based on nuclear content. Specifically, AO has a natural affinity for nucleic acids, so it can stain DNA and RNA of live cells.[38] When excited under blue light, DNA emits green and RNA emits red, which enables the classification of sub-types using one nuclear dye. Based on this methodology, lymphocytes emit an intense green, granulocytes emit mostly red, and monocytes emit a moderate amount of both green and red—all under blue excitation.

2.2 Custom-built fluorescent microscope

To image the buffy coat, a fluorescent microscope was developed for use with AO stain. The system, as pictured in Fig. 2(a), is mounted on two linear stages (LSM025A and LSA25A, Zaber) to provide translation along y and z. The excitation optics include a blue LED (CreeXPE-Blu-1, LED Supply), excitation filter (475 ± 35 nm, Semrock), condenser lens (f = 8 mm, ACL12708U, Thorlabs), dichroic mirror (506 nm beam splitter, Semrock), and an objective lens (Olympus Achromatic, Thorlabs). For capillary tube experiments, a 4× objective (0.1 NA, RMS4×) was used, whereas a 10× objective (0.25 NA, RMS10×) was used for acrylic chip experiments due to sizing and sample volume differences between the two methods.

After illuminating the sample, the reflected light passes back through the objective lens and dichroic mirror, and then reflects off a right-angled mirror to redirect the light through a tube lens (f = 50 mm, AC127050A, Thorlabs). Next, the light passes through a motorized filter-wheel which rotates a green (529 ± 24 nm, Semrock) and red (684 ± 24 nm, Semrock) filter in front of the camera. The filter wheel is actuated *via* a DC-brushed gearmotor (GM22, Solarbotics) using an H-bridge motor driver circuit (COM-00315, SparkFun Electronics).

As seen in Fig. 2(b), the filter wheel contains a motor mount, filter holder, and support brackets—all rapid prototyped out of ABS plastic. The motor mount also contains slots for two Hall effect sensors (A1120, Allegro MicroSystems). Embedding a small magnet (D101-N52, K&J Magnetics) in the filter holder, the green and red filters can be alternated using a switching control scheme. Finally, the filtered light is captured by a CMOS monochrome camera (FMVU-03MTM-CS, Point Grey), which transmits captured images to the host processor (Intel i5-2450M CPU) for analysis.

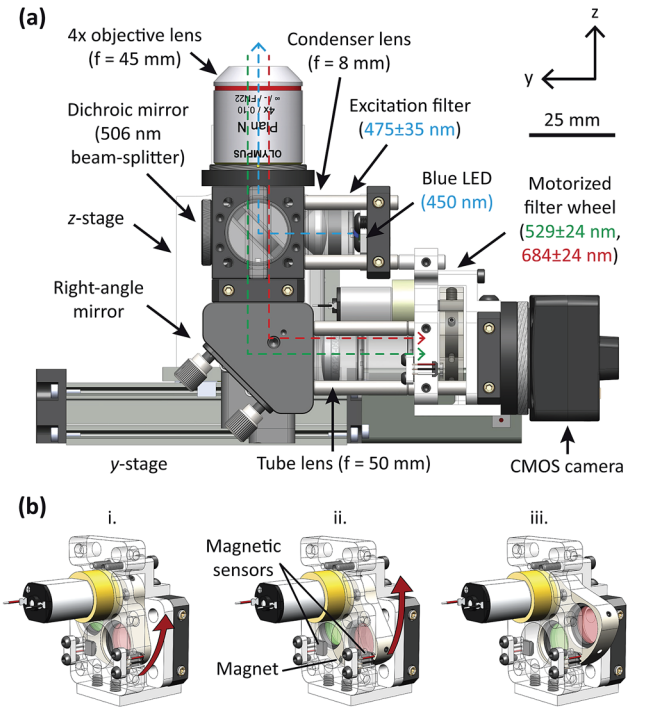

Fig. 2 Custom-built fluorescent microscope. (a) Conceptual design of the microscope, highlighting key components in the system. Dotted lines indicate excitation (blue) and emission (green/red) light paths. (b) Illustration of the motorized filter wheel mechanism: (i) red filter positioned in light path; (ii) filter wheel rotating until magnetic sensor is triggered; and (iii) green filter positioned in light path.

2.3 Glass capillary tube testing

Glass capillary tubes pre-stained with AO (23-900-105, Fisher Scientific) were used for the first set of experiments to evaluate the microscope and bulk-cell analysis approach. This product included a plastic float, which was placed in the tube after pipetting in the sample. Use of the plastic float expands the buffy coat tenfold for enhanced visualization.[37] Porcine blood sample controls (424304 and 424305, Drucker) were used to establish standard curves for lym/mon, gran, and absolute leukocyte counts. Blood cells in porcine and human samples have similar densities, which allows us to test the feasibility of the centrifugation approach. In total, 48 trials were performed (*i.e.*, 4 control levels × 3 replicates × 4 tube orientations).

The experimental protocol was as follows. First, 70 μl of blood was pipetted into the capillary tube and then the tube was inverted six times to ensure adequate mixing. Next, the plastic float was inserted and the bottom of the tube was capped with a rubber stopper. To fractionate the sample, tubes were placed in 15 ml vials, which were then spun in a bench-top centrifuge (Allegra X-22R, Beckman Coulter) for 5 min at 1500 RCF.

2.3.1 Image acquisition and processing. To image the buffy coat, capillary tubes were mounted on a test stand above the microscope (Fig. 3(a)). Motorized stages, as seen in Fig. 2, were then adjusted through a program written in LabVIEW to obtain a clear image of the fluorescing white cell region. Images were acquired along the full length of the tube and stitched together post-testing in Matlab. Four sets of images were acquired along

different tube orientations (in 90° increments) to analyze intra-run variability in the buffy coat measurements.

Image processing was then performed to quantify the fluorescing regions in the green and red channel images (Fig. 3(c and d)). Beginning with the grayscale green channel image, the buffy coat was cropped and intensity values were adjusted *via* linear contrast stretching. A global threshold was then applied using Otsu's method,[39] and morphological operations were used to remove small pixel groups. Fig. 3(c)ii shows the segmented border overlayed on the original image.

Next, to isolate the gran layer, the segmented region in the green channel was used as a mask in the red channel, preventing the lym/mon layer from interfering with the gran segmentation. Similar to the previous segmentation step, a global threshold was then applied. In this case, however, minimal morphological operations were used in order to preserve cell clumps that may have drifted away from the gran layer. The resulting segmentation is displayed in Fig. 3(d)ii.

Once the lym/mon and gran layers were segmented, pixel areas were quantified and plotted against measured cell counts to generate standard curves. Cell counts were measured using the QBC Star Analyzer ($n = 3$) and the accuracy of the cell counts was compared against measurements from a flow cytometer (Abbott CD-3700, $n = 3$). A more detailed description of the image processing routine and the corresponding Matlab code, is provided in the ESI.†

2.4 Acrylic chip testing

In the next experiments, we developed acrylic chips and spun them on a mini-centrifuge. Chips were fabricated using two layers of 1.5 mm-thick cast acrylic sheets (8560K171, McMaster-Carr) and 100 μm-thick pressure sensitive adhesive (PSA) film (DFM 100, FLEXcon) sandwiched in between (Fig. 4(a)). The acrylic sheets were cut using a laser engraver (Zing 24, 60 W, Epilog), whereas channels in the PSA were shaped with a vinyl cutter (SV-8, Roland DGA). The acrylic pieces were surface treated *via* corona discharge (BD-10A, Electro-Technic) to enhance wettability. Top and bottom layers were then aligned and bonded using a heat press (Clam shell, PowerPress). Altogether, the raw materials cost is <$0.10 per chip.

The design contains an inlet and air vent in the top layer (Fig. 4(b)). When manually pipetting in the sample, it fills the inlet reservoir *via* capillary action until the air vent is blocked by the fluid. A capillary valve below the inlet reservoir prevents blood from flowing into the sedimentation channel. The combination of the valve and air vent allows the inlet reservoir to trap 5 μl of sample. Upon centrifugation, the centrifugal force (F_c) exceeds the forces due to surface tension (F_s), allowing the sample to pass through the valve at approximately 1700 rpm. The sedimentation channel width was selected to be 1 mm so that approximately 85% of the channel width could be within the microscope's field-of-view using a 10× objective lens.

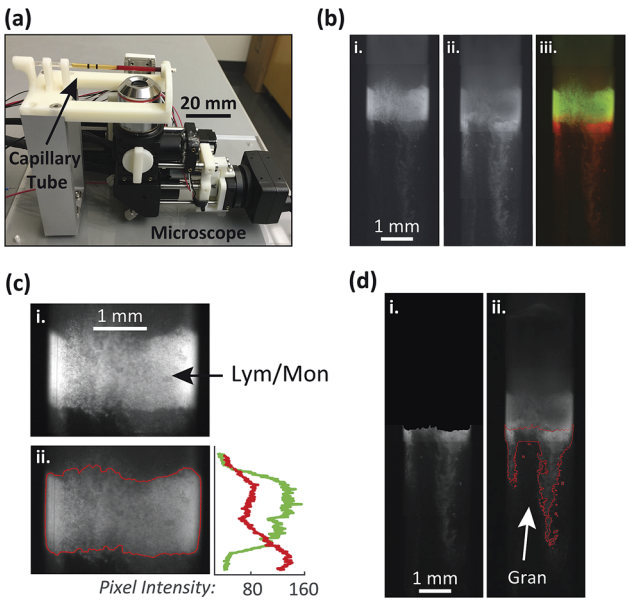

Fig. 3 Buffy coat image acquisition and processing in capillary tubes. (a) Imaging test platform. (b) Grayscale images from the (i) green and (ii) red channels, with (iii) displaying the merged image. (c) Processing of green channel image, including: (i) cropping and (ii) segmentation (intensity profile used to separate lym from mon). (d) Processing of red channel image, including: (i) masking out the lym/mon layer and (ii) segmentation.

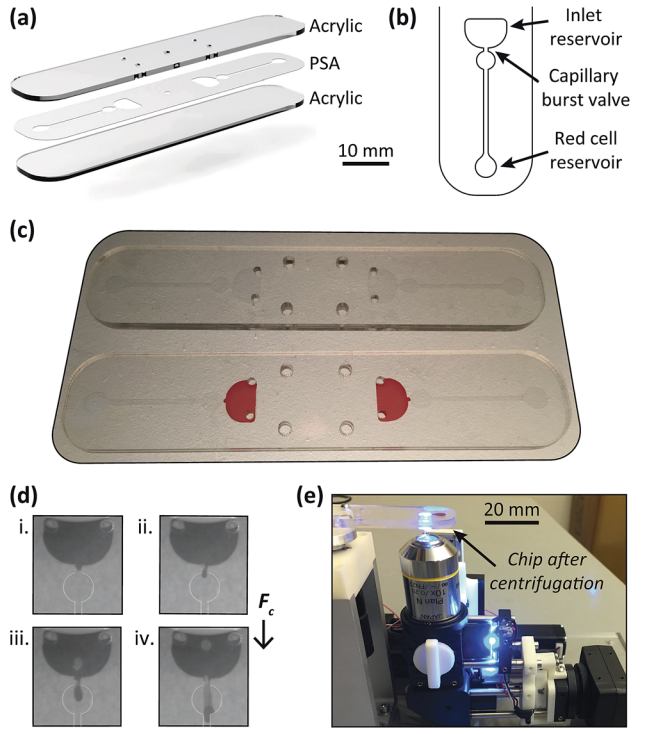

Fig. 4 Acrylic chip testing. (a) Three-layer design—top and bottom: acrylic; middle: PSA. (b) Channel layer consists of an inlet reservoir (5 μl volume), capillary burst valve, sedimentation channel, and red cell collection reservoir. (c) Assembled chip (top); blood sample introduced into the inlet reservoir (bottom). (d) Image sequence of capillary burst valve (channel edges highlighted for clarity): (i) and (ii) sample held in inlet ($F_c < F_s$); (iii) and (iv) valve bursts ($F_c > F_c$) and sample flows into sedimentation channel (width: 1 mm). (e) Experimental setup showing the microscope imaging the chip after centrifugation.

In these experiments, a miniature centrifuge was integrated with the microscope (Fig. 4(e)). The centrifuge was driven by a brushless servo (EC-16, 400161, Maxon Motors) which contains a mounting hub to securely attach the acrylic chip. A secondary camera (GS3-U3-32S4M-C, Point Grey) and strobe light (DT-311A, Shimpo) were positioned above the centrifuge for real-time monitoring of fluid flow in the channels.

As in the capillary tube experiments, porcine blood sample controls were used for testing; but in this case, samples were manually stained with AO off-chip and no float was used. Also, a lower sample volume of 5 μl was used with the acrylic chips, because of the thin PSA layer (100 μm) and 1 mm wide sedimentation channel. Fig. 4(c) depicts the assembled chip before and after pipetting in the sample.

2.4.1 Image acquisition and processing. Following centrifugation, the detection channel of the acrylic chip was aligned with the microscope, and the image was focused by adjusting the motorized stages in the LabVIEW interface. A series of images were then acquired along the length of the channel in set increments using a pre-programmed routine (only one image set was acquired for each run). Similar to the image processing scheme used for capillary tube experiments, green and red channel images were stitched together in Matlab.

A global threshold was again applied to extract and measure the lym/mon layer from the green channel image, however in this case, we used a different approach to quantify the granulocytes. Since granulocytes tended to drift-off into the packed red cell layer (even more pronounced with small sample volumes) it can be challenging to reliably segment a region of cells. Instead, we used a summation of pixels approach in the red channel image to quantify granulocytes—a simplified method in which the intensities of each pixel are summed together to produce a total intensity value describing the level of fluorescence.

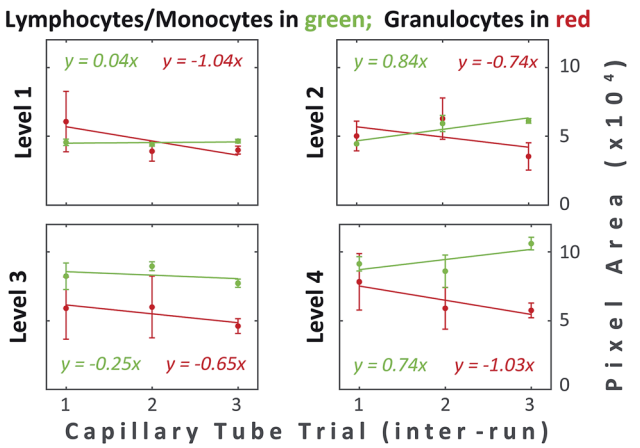

Fig. 5 Variability in buffy coat measurements in capillary tubes. 4 image sets were captured for each tube. Data represent the mean segmented area; error bars represent SD ($n = 4$). Linear fits show inter-run variability due to different tubes/samples used for each control level and error bars show intra-run variability due to tube orientation.

3 Experimental results

3.1 Glass capillary tube testing

Computing the intra-run standard deviation for each experimental trial, little variability was observed in the lym/mon pixel area. However, there was a substantial amount of variability in the granulocyte pixel area based on the orientation of the tube (Fig. 5). Granulocytes had a tendency to clump to one side of the tube, resulting in a radially non-uniform distribution. This motivated our decision to image on all four sides of the tube when extracting data to generate standard curves. Imaging on only one side, like the QBC analyzer does, can give misleading granulocyte counts if it happens to be the wrong side.

Analyzing the standard curves in Fig. 6, the linear regressions demonstrate strong linear fits between pixel areas and measured cell counts (*i.e.*, $r^2 = 0.993$, 0.990, and 0.994 for lym/mon, gran, and total WBCs respectively).

Furthermore, we attempted to isolate lymphocytes from monocytes by analyzing the pixel intensities from the green and red channel images within the segmented lym/mon layer. These sub-types exhibit different proportions of DNA and RNA, and will thus fluoresce differently when stained with AO. Lymphocytes emit more green when excited under blue light compared to monocytes, whereas monocytes also emit a moderate amount of red. We investigated a clustering technique based on Gaussian mixture models (GMM) to separate the two groups of cells based on their chemical fluorescence profile. GMM

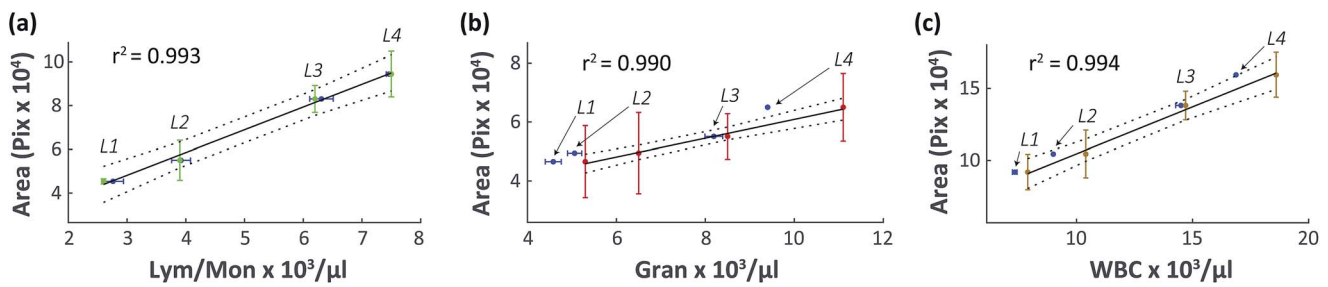

Fig. 6 Capillary tube standard curves for (a) lym/mon, (b) gran, and (c) total WBCs. Buffy coat areas plotted on the y-axes (mean of $n = 12 : 3$ samples per level, 4 tube orientations; error bars represent SD) are compared against measured cell counts using the QBC Analyzer plotted on the x-axes. For the control samples (labeled L1–4), solid and dotted black lines represent linear fits and 95% CIs respectively. Accuracy of cell counts was compared against flow cytometry measurements plotted on the x-axes (blue points, mean of $n = 3$, error bars represent SD).

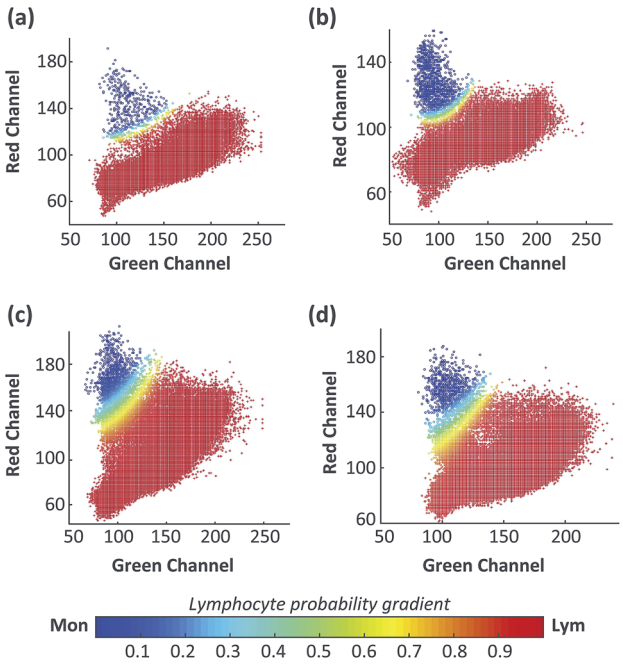

Fig. 7 Representative scatter plots of green and red channel image pixel intensities for blood control levels 1–4 (a–d) using capillary tubes. A GMM was implemented for data clustering to separate mon regions (blue) from lym regions (red). Color map shows the posterior probability of each pixel data point assigned to the lym cluster.

Table 1 Estimated monocytes computed *via* pixel clustering, compared to measured values *via* flow cytometry (cells × 10 per μl)

	Level 1	Level 2	Level 3	Level 4
Estimated	7.4	12.4	22.6	7.7
Measured	5 ± 2	7 ± 4	5 ± 1	7 ± 3

operates by assigning every data point to a cluster by maximizing component posterior probability.[40] Results are displayed in Fig. 7 (n = 1), with heat maps indicating the likelihood of a pixel belonging to the lymphocyte cluster. Table 1 summarizes the results, indicating the number of monocytes in each control sample estimated *via* pixel clustering in comparison to measured cell counts *via* flow cytometry.

3.2 Acrylic chip testing

As we discovered in the previous experiments, imaging on only one side of the capillary tube can give misleading cell counts if it happens to be the wrong side. By housing the sample within a flat, rectangular channel, the need to repeatedly rotate and image the tube is avoided. Additionally, imaging on a flat plane avoids having different focusing distances, as was encountered in the round capillary tubes.

During the acrylic chip testing, granulocytes tended to drift off into the packed red cell layer considerably more than those from the capillary tube experiments. This introduced a significant amount of noise when trying to quantify the granulocytes through segmentation. Instead, we used a summation of pixels approach which worked well in estimating the number of granulocytes in each sample. After masking out the lym/mon region and areas above, the remaining fluorescence observed in the red channel was assumed to be from the granulocytes.

Standard curves obtained from analyzing samples on the acrylic chips are displayed in Fig. 8, where the results show strong linear fits (*i.e.*, r^2 = 0.979, 0.947, and 0.961 for lym/mon, gran, and total WBCs respectively). However, more variability is observed compared to results obtained using capillary tubes. Possible explanations for the increased variability include: the lack of a float to expand the buffy coat, low-sample volumes, and poor separation between blood cell layers.

4 Discussion

In this paper, we demonstrated two methods for differential leukocyte counting using a bulk-cell analysis approach. We also presented preliminary evidence for isolating lymphocytes from monocytes and obtaining a 3-part differential by analyzing pixel intensities in the green and red channel images.

More accurate and repeatable leukocyte counts were observed in the capillary tube control compared to the acrylic chip group. However, capillary tubes required larger sample volumes (*i.e.*, 70 μl *vs.* 5 μl per test) and more expensive consumables from a raw materials standpoint. Specifically, the

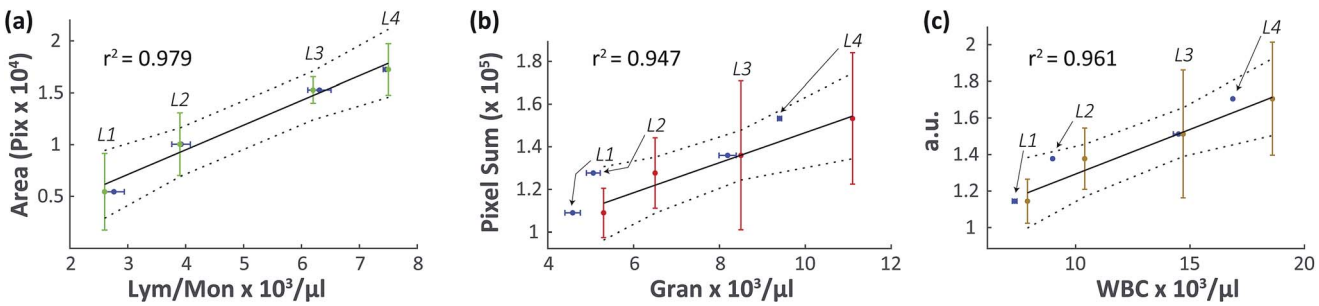

Fig. 8 Acrylic chip standard curves for (a) lym/mon, (b) gran, and (c) total WBCs (a.u. indicates the summation of pixel areas and intensities from the lym/mon and gran data respectively). Buffy coat measurements (mean of n = 3, error bars represent SD) are compared against measured cell counts using the QBC Analyzer. For the control samples (labeled L1–4), solid and dotted black lines represent linear fits and 95% CIs respectively. Accuracy of cell counts was compared against flow cytometry measurements (blue points, mean of n = 3, error bars represent SD).

cost of one capillary tube could range from $1.15 to $5.75, based on an 80% or 0% profit margin respectively from the listed price.[36] Conversely, the raw materials cost for one acrylic chip is $0.10. Additionally, the acrylic chips provided a flat imaging plane for measuring the buffy coat and a simple design that can easily be modified to enhance leukocyte spreading, and thus, improve cell count accuracy and repeatability. The manufacturing process to produce these devices is highly automated through the use of a laser and vinyl cutter. Using this process, it takes approximately 10 and 20 seconds to cut one layer of acrylic and PSA respectively. In one hour, 360 acrylic chips and 175 PSA layers can be produced with our current setup. For scaling, industrial cutters can be used that have larger workspaces and faster operating times.

Nevertheless, several limitations with the bulk-cell analysis approach remain. As previously mentioned, the capillary tube method allowed misleading cell counts due to imaging on only one side of the tube—the curved surface of which also required different focusing distances. Our solution was to fabricate a flat acrylic chip, excluding a plastic float: the trade-off being that granulocytes could spread evenly without clumping around the float, but at the expense of not expanding the buffy layer. In future work, we could instead use a density medium to better isolate the granulocytes from the packed red cell layer.

Altogether, this work demonstrates a simple, reliable method to rapidly obtain differential leukocyte counts with minimal sample preparation in a portable unit.

Acknowledgements

This research was supported by a grant from the NIH (R01EB020036). The work of M. Balter was supported by an NSF Graduate Fellowship (DGE-0937373). The work of A. Chen was supported by an NIH F31 Predoctoral Fellowship (EB018191).

References

1 B. A. Kidd, G. Hoffman, N. Zimmerman, L. Li, J. W. Morgan, P. K. Glowe, G. J. Botwin, S. Parekh, N. Babic, M. W. Doust, G. B. Stock, E. E. Schadt and J. T. Dudley, *J. Clin. Invest.*, 2016, **1**, 1–11.
2 The Freedonia Group, *U.S. In vitro diagnostics*, 2011, vol. 59.
3 J. Hammerling, *Lab. Med.*, 2012, **43**, 41–44.
4 C. Chin, V. Linder and S. Sia, *Lab Chip*, 2012, **12**, 2118–2134.
5 E. Hing, M. Hall, J. Ashman and J. Xu, *National Hospital Ambulatory Medical Care Survey: 2007 outpatient department summary*, 2010.
6 E. Lee-Lewandrowski, K. Gregory and K. Lewandrowski, *Clin. Chim. Acta*, 2010, **411**, 1799–1805.
7 M. M. Johnson and K. B. Lewandrowski, *Point of Care*, 2007, **6**, 134–138.
8 J. Ducrée, S. Haeberle, S. Lutz, S. Pausch, F. V. Stetten and R. Zengerle, *J. Micromech. Microeng.*, 2007, **17**, S103–S115.
9 R. Gorkin, J. Park, J. Siegrist, M. Amasia, B. S. Lee, J.-M. Park, J. Kim, H. Kim, M. Madou and Y.-K. Cho, *Lab Chip*, 2010, **10**, 1758–1773.
10 M. Madou, J. Zoval, G. Jia, H. Kido, J. Kim and N. Kim, *Annu. Rev. Biomed. Eng.*, 2006, **8**, 601–628.
11 T. van Oordt, Y. Barb, J. Smetana, R. Zengerle and F. von Stetten, *Lab Chip*, 2013, **13**, 2888–2892.
12 M. Amasia and M. Madou, *Bioanalysis*, 2010, **2**, 1701–1710.
13 R. Burger, N. Reis, J. G. da Fonseca and J. Ducrée, *J. Micromech. Microeng.*, 2013, **23**, 1–5.
14 N. Godino, R. Gorkin, A. V. Linares, R. Burger and J. Ducrée, *Lab Chip*, 2013, **13**, 685–694.
15 F. Schwemmer, S. Zehnle, D. Mark, F. von Stetten, R. Zengerle and N. Paust, *Lab Chip*, 2015, **15**, 1545–1553.
16 J. Steigert, T. Brenner, M. Grumann, L. Riegger, S. Lutz, R. Zengerle and J. Ducrée, *Biomed. Microdevices*, 2007, **9**, 675–679.
17 J. M. Chen, P. C. Huang and M. G. Lin, *Microfluid. Nanofluid.*, 2008, **4**, 427–437.
18 S. Haeberle, T. Brenner, H. P. Schlosser, R. Zengerle and J. Ducrée, *Chem. Eng. Technol.*, 2005, **28**, 613–616.
19 R. Burger, L. Amato and A. Boisen, *Biosens. Bioelectron.*, 2016, **76**, 1–14.
20 J. Steigert, M. Grumann, T. Brenner, L. Riegger, J. Harter, R. Zengerle and J. Ducrée, *Lab Chip*, 2006, **6**, 1040–1044.
21 C. E. Nwankire, M. Czugala, R. Burger, K. J. Fraser, T. M. Connell, T. Glennon, B. E. Onwuliri, I. E. Nduaguibe, D. Diamond and J. Ducrée, *Biosens. Bioelectron.*, 2014, **56**, 352–358.
22 B. S. Lee, J.-N. Lee, J.-M. Park, J.-G. Lee, S. Kim, Y.-K. Cho and C. Ko, *Lab Chip*, 2009, **9**, 1548–1555.
23 J. Park, V. Sunkara, T. H. Kim, H. Hwang and Y. K. Cho, *Anal. Chem.*, 2012, **84**, 2133–2140.
24 F. Stumpf, F. Schwemmer, T. Hutzenlaub, D. Baumann, O. Strohmeier, G. Dingemanns, G. Simons, C. Sager, L. Plobner, F. von Stetten, R. Zengerle and D. Mark, *Lab Chip*, 2016, **16**, 199–207.
25 a. Kloke, a. R. Fiebach, S. Zhang, L. Drechsel, S. Niekrawietz, M. M. Hoehl, R. Kneusel, K. Panthel, J. Steigert, F. von Stetten, R. Zengerle and N. Paust, *Lab Chip*, 2014, **14**, 1527–1537.
26 M. Glynn, C. Nwankire, K. Lemass, D. Kinahan and J. Ducrée, *Microsystems & Nanoengineering*, 2015, **1**, 1–9.
27 M. Glynn, D. Kirby, D. Chung, D. J. Kinahan, G. Kijanka and J. Ducrée, *J. Lab. Autom.*, 2013, **19**, 285–296.
28 Abaxis, Piccolo Xpress, 2015, http://www.piccoloxpress.com.
29 Samsung, LabGEO IB10, 2016, http://www.samsung.com.
30 O. Strohmeier, M. Keller, F. Schwemmer, S. Zehnle, D. Mark, F. von Stetten, R. Zengerle and N. Paust, *Chem. Soc. Rev.*, 2015, **44**, 6187–6229.
31 H. Shiono and Y. Ito, *Prep. Biochem. Biotechnol.*, 2003, **33**, 87–100.
32 U. Y. Schaff, A. M. Tentori and G. J. Sommer, *Int. Conf. Miniaturized Syst. Chem. Life Sci.*, 14th, 2010, pp. 103–105.
33 D. J. Kinahan, S. M. Kearney, N. A. Kilcawley, P. L. Early, M. T. Glynn and J. Ducrée, *PLoS One*, 2016, **11**, 1–13.
34 HemoCue, HemoCue WBC System, 2016, http://www.hemocue.com.
35 H. Russcher, N. V. Deursen, T. Ermens and R. D. Jonge, *Ned Tijdschr Klin Chem Labgeneesk*, 2013, **38**, 140–141.

36 B. R. A. Levine, *Clinical Issues*, 2013, pp. 14–17.
37 O. Erhabor, G. Richardson, I. Mohammed, C. Thorton, J. Bark, M. Hurst, D. Hamer and P. Kinsella, *Br. J. Biomed. Sci.*, 2013, **70**, 67–74.
38 S. Janhanmehr, K. Hyde, C. Geary, K. Cinkotai and J. Maciver, *J. Clin. Pathol.*, 1987, 926–929.
39 N. Otsu, *IEEE Trans. Syst. Man. Cybern. Syst. Hum.*, 1979, **20**, 62–66.
40 G. McLachlan and D. Peel, *Finite Mixture Models*, 2000, pp. 238–256.